

## A methodology for fast finite element modeling of electrostatically actuated MEMS

Prasad S. Sumant<sup>1,\*</sup>, Narayana R. Aluru<sup>1</sup> and Andreas C. Cangellaris<sup>2</sup>

<sup>1</sup>*Department of Mechanical Science and Engineering, University of Illinois, 1206 W. Green St., Urbana, IL 61801, U.S.A.*

<sup>2</sup>*Department of Electrical and Computer Engineering, University of Illinois, 1406 W. Green St., Urbana, IL 61801, U.S.A.*

### SUMMARY

In this paper, a methodology is proposed for expediting the coupled electro-mechanical finite element modeling of electrostatically actuated MEMS. The proposed methodology eliminates the need for repeated finite element meshing and subsequent electrostatic modeling of the device during mechanical deformation. We achieve this by using an approximation of the charge density on the movable electrode in the deformed geometry in terms of the charge density in the non-deformed geometry and displacements of the movable electrode. The electrostatic problem has to be solved only once and thus this method speeds up the coupled electro-mechanical simulation process. The proposed methodology is demonstrated through its application to the modeling of four MEMS devices with varying length-to-gap ratios, multiple dielectrics and complicated geometries. Its accuracy is assessed through comparisons of its results with results obtained using both analytical solutions and finite element solutions obtained using ANSYS. Copyright © 2008 John Wiley & Sons, Ltd.

Received 9 September 2007; Revised 3 August 2008; Accepted 16 August 2008

KEY WORDS: MEMS; modeling; FEM; electrostatic actuation

### 1. INTRODUCTION

Micro-electro-mechanical (MEM) devices like switches, varactors and oscillators have shown great potential for use in communication devices, sensors and actuators [1, 2]. Typically, they consist of thin, movable beams or electrodes suspended over a fixed electrode. Application of a voltage between the movable and fixed electrodes results in electrode movement and/or deformation that

\*Correspondence to: Prasad S. Sumant, Department of Mechanical Science and Engineering, University of Illinois, 1206 W. Green St., Urbana, IL 61801, U.S.A.

†E-mail: psumant2@uiuc.edu

Contract/grant sponsor: Defense Advanced Research Projects Agency (DARPA)

can be exploited for the purposes of actuation, switching, sensing and numerous other signal and information processing functions. In order to maximize movement while keeping the actuation voltage low, the movable beams are typically made of very thin metal films with high aspect ratios. In addition, the gap between movable and fixed electrodes is kept sufficiently small to provide for large electrostatic forces under low actuation voltages. Multiple layers of insulating dielectric may be incorporated in the space between the electrodes to enhance performance and improve device reliability. Long-term device reliability is further enhanced through the incorporation of special features in the geometry of the electrodes, such as holes or protrusions.

The widespread insertion of MEMS devices in integrated electronics is critically dependent on the availability of accurate and computationally efficient, multi-physics CAD tools in support of device design iteration, optimization and performance degradation assessment. In support of the latter, the multi-physics modeling must comprehend all mechanisms that contribute to performance degradation. For example, in the case of RF MEMS capacitive switches the impact of charge accumulation in the insulating dielectric on the performance of the switch must be accurately quantified to enable the reliable operation of the switch [3].

A detailed characterization of an electrostatically actuated MEMS device such as the aforementioned RF MEMS capacitive switch requires the solution of a coupled electro-mechanical problem that comprehends the movable electrodes and their support if any, as well as the potentially inhomogeneous media occupying the volume between the movable and fixed electrodes. Several one-dimensional models and approximate analytical expressions have been presented for calculating the electro-mechanical response of the switch [4]. There also have been some efforts towards the development of one-dimensional models for reliability analysis [5]. Such models serve as a good starting point for the design process and provide for the development of an intuitive understanding of the operation of the device. However, these methods are limited in their description of the governing physics and, hence, unable to support the modeling detail and simulation accuracy needed for design optimization and performance degradation assessment. To provide for the needed modeling rigor and solution accuracy, finite element methods (FEM), boundary elements methods (BEM) and hybrid FEM–BEM schemes are used. For example, MEMCAD [6] uses ABAQUS, a commercial FEM package for the mechanical analysis and a BEM-based program FASTCAP [7] for the electrostatic analysis. In the absence of material inhomogeneity, BEM is the method of choice for the electrostatic problem, since only the surface of the conducting electrodes need be discretized. However, for devices with significant dielectric material inhomogeneity and, in general, substantial geometric complexity, an FEM solution to the electrostatic problem offers modeling versatility and formulation simplicity. To avoid the numerical error introduced by the truncation of the finite element grid for the case of unbounded geometries, hybrid formulations where an FEM model of the interior is complemented by a BEM statement on the surface used for truncating the computational domain is possible [8, 9].

For the purposes of this paper it is assumed that the material complexity of the MEMS device under consideration is such that an FEM solution of the electrostatic boundary value problem (BVP) is preferable. Apart from the discretization of the computational domain for the solution of the electrostatic BVP, there are additional computational challenges inherent to the coupled electro-mechanical analysis.

To provide a framework for their discussion, let us consider the application of an FEM model for a coupled electro-mechanical analysis of an electrostatically actuated MEMS device. In order to keep the presentation simple, it is assumed that a relaxation-based algorithm rather than a Newton method [10] is used for the coupling of the electrostatic and the mechanical domains. The

relaxation-based algorithm is as follows:

*Algorithm 1*

Perform an electrostatic analysis in the non-deformed geometry to calculate forces for use in the mechanical domain.

**Repeat** the following **until** an equilibrium state is reached:

1. Perform mechanical analysis (in the non-deformed geometry) to compute structural displacements.
2. Update the geometry of the movable electrode using computed displacements.
3. Compute the electric field by electrostatic analysis (deformed geometry).
4. Compute electrostatic forces on the movable membrane in the deformed configuration.
5. Transform the electrostatic forces to the original non-deformed configuration.

During each step of the relaxation-based algorithm the beam deforms modifying the electrostatic BVP domain. In the context of BEM, a Lagrangian formulation was proposed in [11] to eliminate the need for such geometry update. In the context of FEM, the geometry update necessitates a change in the mesh used for the finite element solution of the electrostatic BVP. This is depicted for the case of the cantilever beam electrode suspended over a fixed bottom electrode in Figure 1. To update the finite element mesh for the deformed geometry one approach is to treat the mesh as another elastic solid with some appropriate elastic properties, and use the deflection of the movable beam as input boundary displacements [12, 13]. Then, using a finite element solution to the elasticity problem, the new mesh is obtained as a displacement of the previous one. This process is also known as mesh updating or mesh morphing. Similar smoothing techniques are commonly found in commercial FEM software packages such as ANSYS [14]. An alternative approach is to simply re-mesh the deformed structure at each relaxation step. Both approaches contribute an undesirable overhead to the computational cost of the iterative solution.

To avoid re-meshing the Lagrangian formulation of [11, 15] could be adopted, in principle. However, a Lagrangian formulation for FEM will require information about nodal displacements at all points in the electrical mesh, which, from a computational point of view, is not very different from a mesh update. Furthermore, a mesh update using any of the above techniques would require the finite element matrix for the electrostatic BVP to be updated and factored at every relaxation step.

The methodology proposed in this paper is aimed at overcoming the aforementioned shortcomings of the FEM solution of the electrostatic BVP by eliminating the need for mesh update. This paper is organized as follows. In Section 2, the proposed methodology for the solution of the electrostatic BVP without mesh updating is presented. This is followed by the demonstration of the proposed methodology in Section 3 through its application to the modeling of four electrostatically actuated MEMS devices. These numerical studies provide for the validation of the proposed methodology and the assessment of its accuracy. The paper concludes with some remarks about the types of electrostatically actuated MEMS for which the proposed methodology is most suitable for their accurate electro-mechanical analysis.

## 2. PROPOSED METHODOLOGY

### 2.1. Auxiliary electrostatic BVP

The proposed methodology is founded on the idea that the electric flux density on the movable electrode in the deformed configuration can be approximated in terms of the electric flux density

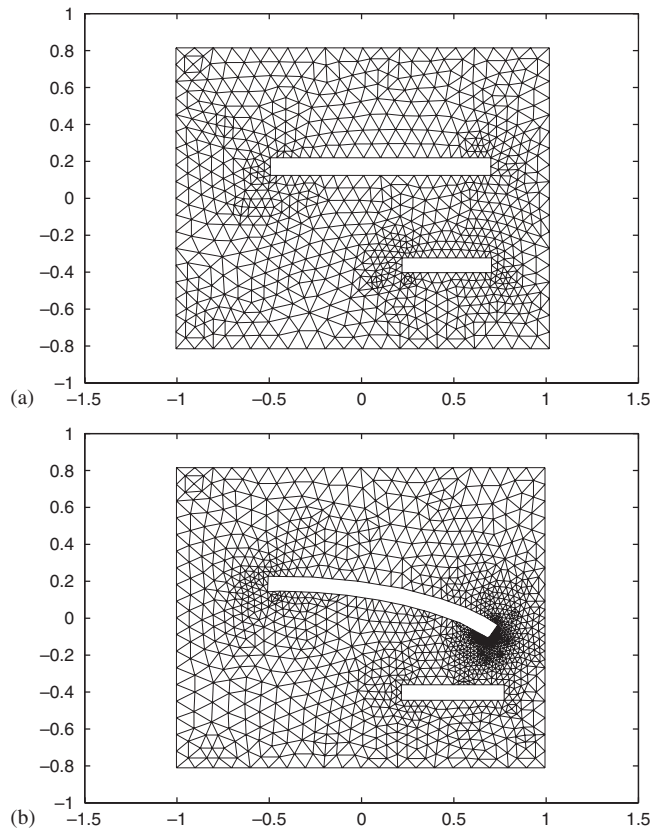


Figure 1. Conventional FEM electro-mechanical modeling: (a) electrostatic BVP meshing of non-deformed configuration and (b) electrostatic BVP meshing of deformed configuration.

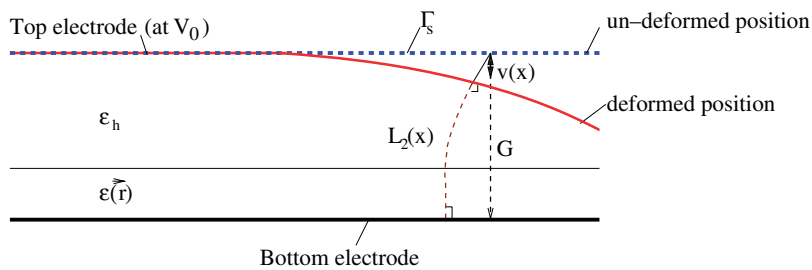


Figure 2. Proposed approach: mapping deformed configuration to undeformed configuration.

on that electrode in the non-deformed configuration and the updated displacement of the movable electrode.

Let us consider the most generic representation of an MEMS device in terms of a movable top electrode, a bottom, fixed electrode, and the in-between region that, in general, is filled with

an inhomogeneous dielectric as shown in Figure 2. To elaborate, as shown in the figure, the region surrounding the moving electrode is taken to be a homogeneous dielectric, (which is, most commonly air or vacuum), and it is represented by  $\epsilon_h$ . The remaining space between the electrodes may be filled with a different dielectric medium, e.g. serving the purpose of an insulation layer between the electrodes. It is represented by  $\epsilon(\mathbf{r})$  in the figure.

Let us consider an intermediate deformed configuration of the top electrode as shown in Figure 2. The coupling between the mechanical and electrical domains happens through the electrostatic pressure,  $P$ , on the movable electrode. It is given by

$$P = \frac{\rho_s^2}{2\epsilon} \quad (1)$$

where the electric charge density on the conductor surface ( $\Gamma_s$ ) is given by

$$\rho_s = \hat{n} \cdot (-\epsilon \nabla \phi) \quad (2)$$

In the above equation  $\hat{n}$  is the outward pointing unit normal on the conductor surface. Using the fact that the electric field intensity  $\mathbf{E} = -\nabla \phi$  has only the normal component on a conductor surface, and using the electric flux density,  $\mathbf{D} = \epsilon \mathbf{E}$ , the electrostatic pressure on the movable electrode is cast in the following form:

$$P = \frac{1}{2\epsilon} |\mathbf{D}|^2 \quad (3)$$

In the deformed configuration, let us consider a flux line  $L_2(x)$  (Figure 2) between the two electrodes starting at the co-ordinate  $x$  along the top electrode. Let  $V_0$  be the potential difference between the two electrodes. Along such a flux line the magnitude of the electric flux density  $\mathbf{D}_{\text{def}}(x)$  is constant. Let it be  $\mathbf{D}_c$ . Hence, we can write,

$$\int_{L_2} \mathbf{E} \cdot d\mathbf{l} = V_0 \quad (4)$$

$$\int_{L_2} \frac{\mathbf{D}_c \cdot d\mathbf{l}}{\epsilon(\mathbf{r})} = V_0 \quad (5)$$

$$|\mathbf{D}_c| \int_{L_2} \frac{1}{\epsilon(\mathbf{r})} dl = V_0 \quad (6)$$

$$|\mathbf{D}_{\text{def}}(x)| = \frac{V_0}{\int_{L_2} \frac{1}{\epsilon(\mathbf{r})} dl} \quad (7)$$

Repeating the above derivation along a flux line  $L(x)$  between the two electrodes in the non-deformed configuration we can write

$$|\mathbf{D}_0(x)| = \frac{V_0}{\int_L \frac{1}{\epsilon(\mathbf{r})} dl} \quad (8)$$

Combining (7) and (8),

$$|\mathbf{D}_{\text{def}}(x)| = \frac{\int_L \frac{1}{\varepsilon(\mathbf{r})} dl}{\int_{L_2} \frac{1}{\varepsilon(\mathbf{r})} dl} |\mathbf{D}_0(x)| \quad (9)$$

$$|\mathbf{D}_{\text{def}}(x)| = \text{ratio} \times |\mathbf{D}_0(x)| \quad (10)$$

It is important to note that there are no approximations introduced in the above equation. This expression relates the charge density in the deformed configuration to the charge density on the movable electrode in the non-deformed configuration. Next, we present two different ways of approximating the ratio in the above equation.

### 2.2. Method 1: using geometry

This method exploits the fact that in many practical designs of electrostatically actuated MEMS devices the lengths of the electrodes are much larger than both the thickness of the electrodes and their separation and that their motion occurs within an electrically homogeneous region of space, which is air or vacuum. For example, length-to-separation ratios of values ranging between 50:1 and 200:1 are very common in practical devices. With this in mind, the following equations are proposed for the approximation of the lengths  $L(x)$  and  $L_2(x)$ :

$$L(x) \approx G \quad (11)$$

$$L_2(x) \approx G - v(x) \quad (12)$$

where  $G$  is the distance between the movable and fixed electrodes in the absence of actuation, while  $v(x)$  is the displacement of the movable electrode at position  $x$  along its axis. Thus, (10) can be written as

$$|\mathbf{D}_{\text{def}}(x)| \approx |\mathbf{D}_0(x)| \frac{G}{G - v(x)} \quad (13)$$

As it will be demonstrated in Section 3, this approximation works very well for MEMS involving cantilevers or simply supported beams with homogeneous dielectrics, especially for devices with electrodes of comparable lengths, where the definition of an electrode-to-electrode separation  $G$  is straightforward from the device geometry. However, there are classes of MEMS devices, such as comb drives and other structures with electrodes of disparate lengths and shapes, involving a more complicated dielectric composition. For such devices the definition of an electrode-to-electrode separation distance  $G$  is more cumbersome or even impossible. To provide for a fully automated process for the calculation of the ‘ratio’ in Equation (10), the following method is proposed.

### 2.3. Method 2: using electric field distribution

This method is prompted by the observation that for the case of devices exhibiting asymmetry in their electrode shapes, lengths and placement and presence of dielectrics, the total length of an electric flux line starting from one electrode and ending on the other will be position-dependent. Thus, a position-dependent separation function,  $G(x)$ , must be defined, understood as the length of different electric flux lines between the electrodes. To provide for the calculation of such a

position-dependent separation distance, use is made of the calculated electric flux density on the movable electrode after the first step of the relaxation process. Recall from above that this electric flux density was denoted as  $\mathbf{D}_0(x)$ . Thus,  $G(x)$  is computed by

$$G(x) = \varepsilon_h \frac{V_0}{|\mathbf{D}_0(x)|} \quad (14)$$

where  $V_0$  is the potential difference between the electrodes and  $\varepsilon_h$  is the electric permittivity next to the movable electrode. The length  $L_2(x)$  is approximated using

$$L_2(x) \approx L(x) - v(x) \quad (15)$$

So, we have, using (8), (14) and (15),

$$\int_L \frac{1}{\varepsilon(\mathbf{r})} dl = \frac{G(x)}{\varepsilon_h} \quad (\text{exact}) \quad (16)$$

$$\int_{L_2} \frac{1}{\varepsilon(\mathbf{r})} dl \approx \int_{L-v} \frac{1}{\varepsilon(\mathbf{r})} dl \quad (17)$$

$$\begin{aligned} \int_{L_2} \frac{1}{\varepsilon(\mathbf{r})} dl &\approx \int_L \frac{1}{\varepsilon(\mathbf{r})} dl - \int_v \frac{1}{\varepsilon(\mathbf{r})} dl \\ &= \frac{G(x)}{\varepsilon_h} - \frac{v(x)}{\varepsilon_h} \end{aligned} \quad (18)$$

Thus, (10) becomes,

$$|\mathbf{D}_{\text{def}}(x)| \approx |\mathbf{D}_0(x)| \frac{G(x)}{G(x) - v(x)} \quad (19)$$

The example geometry of a cantilever beam suspended over a ground electrode of different length, as depicted in Figure 3, helps demonstrate the way  $G(x)$  is computed through the aforementioned methodology. From the computed electric field intensity values along the top movable electrode, it is clear that its value is maximum over the portion of the movable electrode directly above the bottom electrode. The field intensity decays rapidly as we move away from and to the left of the left edge of the bottom electrode. Incorporating this variation in the computation of a position-dependent  $G(x)$  results in the distribution depicted in the bottom plot of Figure 3.

It is evident from the plot that  $G(x)$  remains constant and equal to the physical separation between the two electrodes over the right-end portion of the top beam, which is located above the bottom electrode. As we approach the edge of the bottom electrode,  $G(x)$  starts increasing, eventually assuming very large values at distances sufficiently far away from the left edge of the bottom electrode.

Note that the electric field intensity is bound to exhibit very large values at the edges of the conducting electrodes, as the numerical solution attempts to reproduce the charge density singularity in the neighborhood of the edges. In these cases,  $G(x)$  may assume values much smaller than the value of the physical separation between the two electrodes. To avoid numerical difficulties due to such behavior, we impose a condition that

$$G(x) \geq G \quad (20)$$

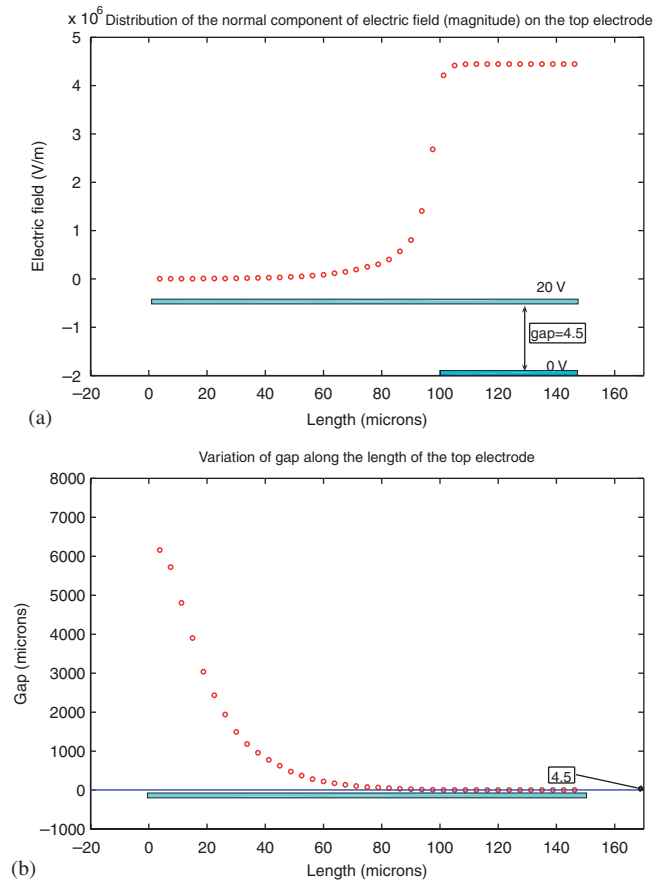


Figure 3.  $G(x)$  calculation using electric field distribution: (a) electric field distribution and (b) position-dependent electrode separation  $G(x)$ .

The algorithm for performing the FEM-based electro-mechanical analysis utilizing the aforementioned approach is as follows:

#### Algorithm 2

1. Solve the electrostatic FEM problem in the non-deformed geometry with constant potential  $V_0$  on the movable electrode ( $\Gamma_s$ ).
2. Using the computed electric field intensity distribution on  $\Gamma_s$ , compute  $G(x)$  for Method 2. For Method 1, skip this step.
3. Loads/boundary conditions for the mechanical solution are computed using the calculated values of the charge density along the movable electrode.
4. Solve the mechanical FEM to compute the deflection/deformation of the movable electrode.
5. Using the calculated displacement  $v(x)$  of the movable electrode, update the charge density along  $\Gamma_s$  using (13) or (19).
6. Go to step 3 and repeat until convergence.

There is no need for re-meshing and re-generating the FEM matrix for the electrostatic BVP. The electrostatic problem is solved only once. This results in computation savings at every relaxation step.

#### 2.4. Computational complexity analysis

In the following we compare the computational complexity of the two algorithms, Algorithm 1 of Section 1 used in the standard FEM electro-mechanical analysis, and Algorithm 2, resulting from the implementation of the methodology proposed in this paper for the FEM solution of the electrostatic BVP. For this purpose, the following notation will be used:

- $N_m$ : number of nodes in the FEM mesh for the mechanical problem.
- $N_e$ : number of nodes in the FEM mesh for the electrostatic problem.
- $N_i$ : number of nodes at the boundary of the movable electrode for the mechanical problem and on  $S_f$  for the auxiliary electrostatic problem.
- $N_{iter}$ : number of relaxation steps for convergence.

Table I summarizes the comparison of the two algorithms. An explanation of the entries in Table I is as follows. For both the algorithms, the stiffness matrix for the mechanical domain needs to be assembled and factored only once. The FEM system for the mechanical domain needs to be solved at every relaxation step for both algorithms. For Algorithm 1, the stiffness matrix for the electrostatic problem needs to be reassembled and factored at every relaxation step as the geometry of the electrostatic problem changes at every step due to electrode deformation. In contrast, in Algorithm 2, this has to be done only once, since the deformed geometry is reflected only in an updated charge density on the fixed surface  $\Gamma_s$ . Furthermore, in Algorithm 1, an FEM mesh update is required at every relaxation step. This cost is completely eliminated in Algorithm 2.

Table I. Computational complexity of Algorithms 1 and 2.

Step	Order	Algorithm 1	Algorithm 2
<i>Assembly</i>			
Stiffness matrix for mechanical domain	$N_m$	1	1
Stiffness matrix for electrical domain	$N_e$	$N_{iter}$	1
Stiffness matrix for pseudo-elastic (electrical) domain	$2N_e$	1	0
<i>Factorization of stiffness matrix</i>			
Stiffness matrix for mechanical domain	$N_m^{1.5}$	1	1
Stiffness matrix for electrical domain	$N_e^{1.5}$	$N_{iter}$	1
Stiffness matrix for pseudo-elastic (electrical) domain	$(2N_e)^{1.5}$	1	0
<i>Forward and backward solve for linear system</i>			
For mechanical domain	$N_m$	$N_{iter}$	$N_{iter}$
For electrical domain	$N_e$	$N_{iter}$	1
For pseudo-elastic (electrical) domain	$(2N_e)$	$N_{iter}$	0
<i>Update interface conditions</i>			
To calculate electrostatic forces for mechanical domain	$N_i$	$N_{iter}$	$N_{iter}$
To calculate mechanical displacements for electrical domain	$N_i$	0	$N_{iter}$
To calculate mechanical displacements for pseudo-elastic domain	$N_i$	$N_{iter}$	0

Assuming  $N_{\text{iter}}=10$ , the computational cost for each algorithm is obtained from the entries of Table I, as follows:

$$\begin{aligned} \text{Algorithm 1: } & O(N_m^{1.5} + 13N_e^{1.5} + 11N_m + 42N_e + 20N_i) \\ & \approx O(N_m^{1.5} + 13N_e^{1.5} + 40N_e) \end{aligned} \quad (21)$$

$$\begin{aligned} \text{Algorithm 2: } & O(N_m^{1.5} + N_e^{1.5} + 11N_m + 2N_e + 20N_i) \\ & \approx O(N_m^{1.5} + N_e^{1.5}) \end{aligned} \quad (22)$$

Thus, Algorithm 2, based on the proposed methodology, is roughly 10 times more efficient than Algorithm 1.

### 3. NUMERICAL STUDIES

Four case studies are presented next for assessing the performance and accuracy of the proposed method and demonstrating its versatility. These studies involve some of the most common electrode geometries used in electrostatically actuated MEMS devices. Each individual case study presents some unique modeling challenges in an effort to examine and quantify the limits of accuracy of the proposed method.

#### 3.1. Cantilever series switch

One of the most important RF MEMS switches is the cantilever series switch [4] depicted in Figure 4(a). It consists of a beam suspended over a bottom ground electrode, which is part of a microwave, planar transmission line. The bottom ground electrode is on top of a silicon substrate. The purpose of this case study is to examine the accuracy of the proposed method in handling cantilever geometries with asymmetric placement of electrodes.

The modeled geometry is depicted in Figure 4(b). Note that the silicon substrate is not included in this study. The top electrode is  $150\mu\text{m}$  in length,  $2\mu\text{m}$  in thickness. Young's modulus  $E$  is 170 GPa and the Poisson ratio  $\nu$  is 0.34. The bottom electrode is  $50\mu\text{m}$  in length,  $2\mu\text{m}$  in thickness, and located  $100\mu\text{m}$  from the leftmost end of the top electrode. The structure was analyzed for different values of the gap length, ranging from 1.5 to  $4.5\mu\text{m}$ . Thus, the length-to-gap ratio (for the top electrode) is varied between 100:1 and 10:1. Recall that in most practical applications, the length-to-gap ratio is kept as high as possible, with length-to-gap ratios between 50:1 and 100:1 being the most common. Hence, the choice of 10:1 as the lower limit of the length-to-gap ratio provides for testing the proposed method beyond the limits of practical geometries for such a class of devices.

Four-node quad elements are used for the mechanical mesh whereas three-node triangles are used for the electrical mesh. ESSOLV macro in ANSYS, which is a sequential coupled field solver, is used for the implementation of Algorithm 1 and for providing the reference solution. For each value of the length of the gap, the applied voltage is varied up to its pull-in value. Figures 5 and 6 depict the computed deflections for four different values of gap length. The proposed methodology

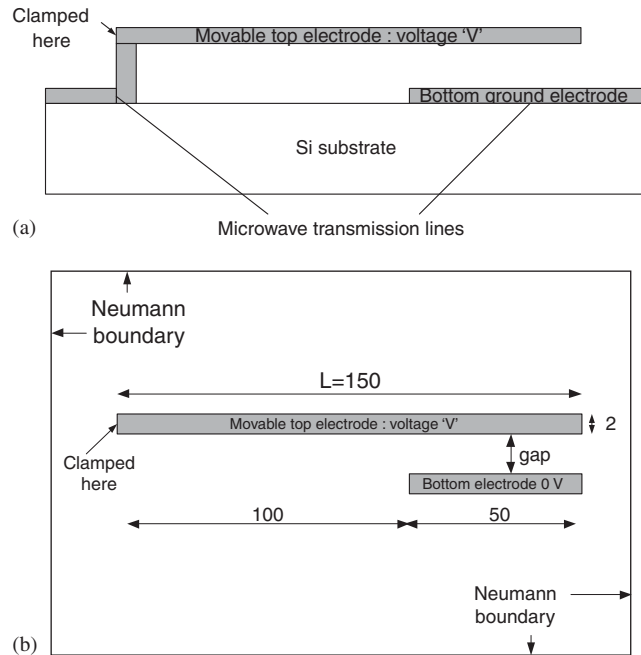


Figure 4. Cantilever series switch: (a) actual device and (b) modeled geometry. All dimensions in microns.

is seen to be very accurate up to pull-in, for both Methods 1 and 2. The results obtained using the proposed methodology remain within 1–2% of the ANSYS results. Figure 7 shows the variation of % error in pull-in with length-to-gap ratios. Even for the extreme case of a length-to-gap ratio of 10:1, the error is found to be less than 3%.

### 3.2. Simply supported RF MEMS capacitive switch

The MEMS device under study in this section is the simply supported RF capacitive switch of [16], depicted in Figure 8. It consists of an Au beam for the top movable electrode, suspended over a center ground conductor, which is part of a coplanar waveguide. The center ground electrode is placed on top of a  $\text{SiO}_2$  layer, which is on top of a silicon substrate. A thin layer of silicon nitride is deposited on top of the center conductor. This layer of dielectric prevents direct metal-to-metal contact of the two electrodes. The presence of the metal posts at which the top beam is attached provide for a natural truncation of the computational domain on the two sides and the top. A truncation boundary is introduced in the Si substrate, resulting in the cross-sectional geometry of the computational domain depicted in Figure 8.

Since the width of the top electrode is much larger than the vertical thickness, a two-dimensional analysis, involving the cross-sectional geometry depicted in Figure 8 suffices. The geometric dimensions that define the cross-sectional geometry are as follows: The length of the top electrode is  $300\ \mu\text{m}$ . Its thickness,  $t$ , is  $0.8\ \mu\text{m}$ . The length of the lower electrode is  $100\ \mu\text{m}$  and its thickness,  $t_e$ , is  $0.8\ \mu\text{m}$ . The silicon oxide layer thickness,  $t_{\text{ox}}$ , is  $0.4\ \mu\text{m}$ . The silicon nitride thickness,  $t_d$ , is

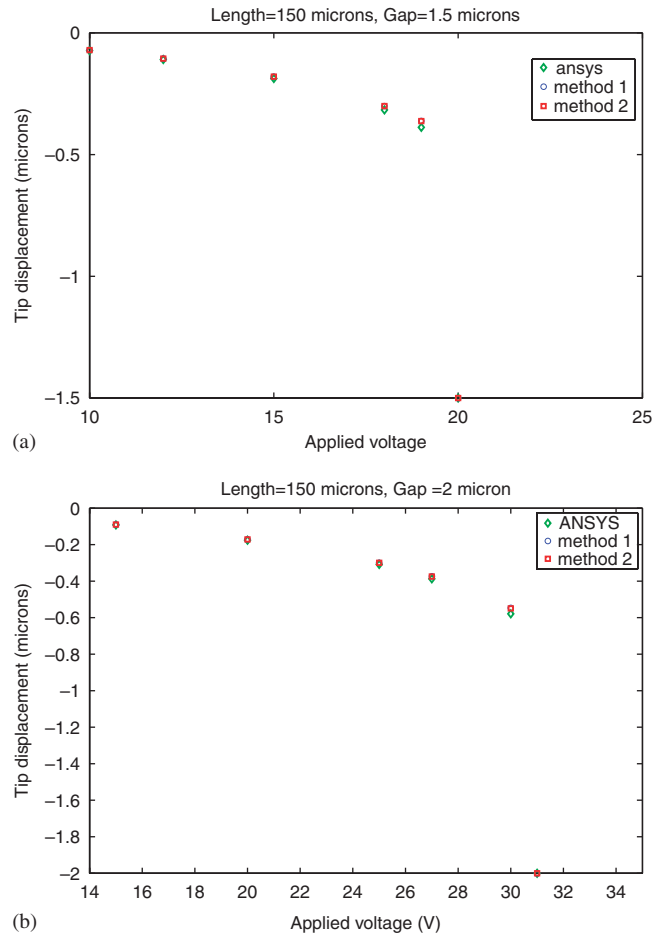


Figure 5. Tip deflection of cantilever: (a) gap length = 1.5  $\mu\text{m}$  and (b) gap length = 2  $\mu\text{m}$ .

0.15  $\mu\text{m}$ . The relative permittivities of the  $\text{Si}_3\text{N}_4$  and  $\text{SiO}_2$  layers are, respectively, 7.6 and 3.9. The relative permittivity of Si is taken to be 11.0. For the Au beam, Young's modulus  $E$  is 80 GPa and the Poisson ratio,  $\nu$ , is 0.42. The thickness of the Si layer is 30  $\mu\text{m}$ . The boundary condition imposed at the bottom truncation boundary for the electrostatic BVP is one of zero electric flux density.

Like in the previous case, we consider designs with different gap lengths,  $g_0$ . The ESSOLV macro in ANSYS is used for generating the reference solution, based on the application of Algorithm 1. For each value of the length of the gap, the applied voltage is varied up to its pull-in value. Figures 9 and 10 depict the computed deflections for four different values of gap length. The proposed methodology is seen to be very accurate up to pull-in, for both Methods 1 and 2. Method 2, in particular, is closer to ANSYS predicted values, as expected, due to its formulation that incorporates dielectrics. The results obtained using the proposed methodology remain within 1% of the ANSYS computed results.

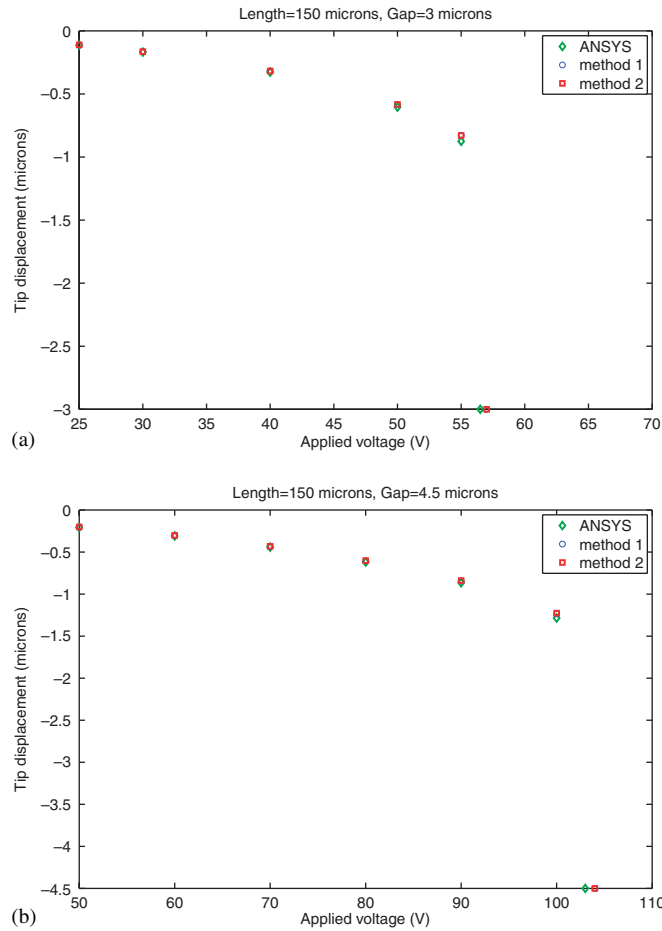


Figure 6. Tip deflection of cantilever: (a) gap length =  $3.0\ \mu\text{m}$  and (b) gap length =  $4.5\ \mu\text{m}$ .

### 3.3. Comb drive

Electrostatically actuated comb drives are an important class of MEMS structures having numerous applications from micro-accelerometers and position controllers to hard disk drive actuators [10, 17, 18]. This case study considers the application of the proposed methodology to the electro-mechanical FEM modeling of the transverse comb drive depicted in Figure 11(a). The system consists of a movable center stage, 24 pairs of interdigitated teeth and four spring beams. The center stage is supported by four folded spring beams anchored at the ends. Electrostatic forces are generated when a voltage is applied between the fixed and movable structures. The movable center stage is  $100\ \mu\text{m}$  long,  $200\ \mu\text{m}$  wide and  $3.7\ \mu\text{m}$  thick. The small and large gaps between the two electrodes are  $g_1 = 2\ \mu\text{m}$  and  $g_2 = 5\ \mu\text{m}$ . The overlap length is  $50\ \mu\text{m}$  and the finger width is  $4\ \mu\text{m}$ . The beam width is  $3\ \mu\text{m}$ , and the lengths of the short and long parts of the folded beam are  $l_1 = 80\ \mu\text{m}$  and  $l_2 = 120\ \mu\text{m}$ , respectively. Young's modulus of the comb structure is  $200\ \text{GPa}$  and

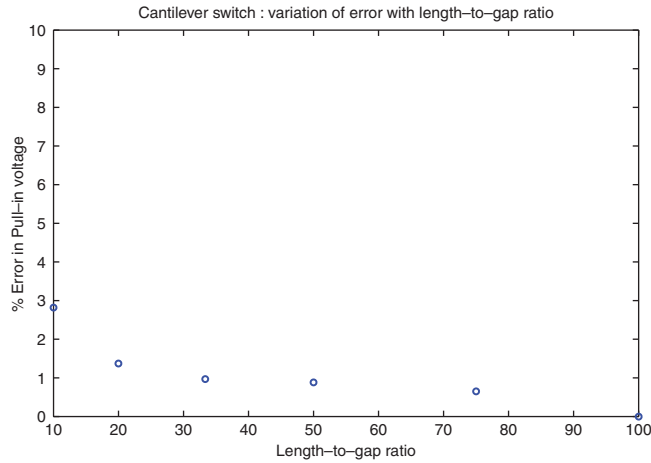


Figure 7. Cantilever switch: % error in pull-in for different length-to-gap ratios.

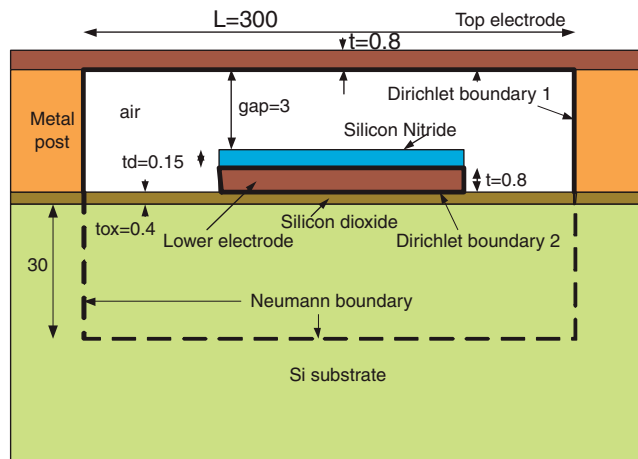


Figure 8. RF MEMS switch. All dimensions in microns.

the Poisson ratio is 0.31. Owing to symmetry, it is sufficient to consider the modeling of just the lower portion, depicted in Figure 11(b). The surrounding medium is assumed to be homogeneous with electric permittivity that of free space as  $\epsilon_0$ .

For small displacements, the displacement of the movable stage can be obtained analytically [17] as

$$\frac{hl_t\epsilon}{2} \left[ \frac{1}{(g_1-x)^2} - \frac{1}{(g_2+x)^2} \right] V^2 = Eh \frac{b^3}{l_1^3+l_2^3} x \tag{23}$$

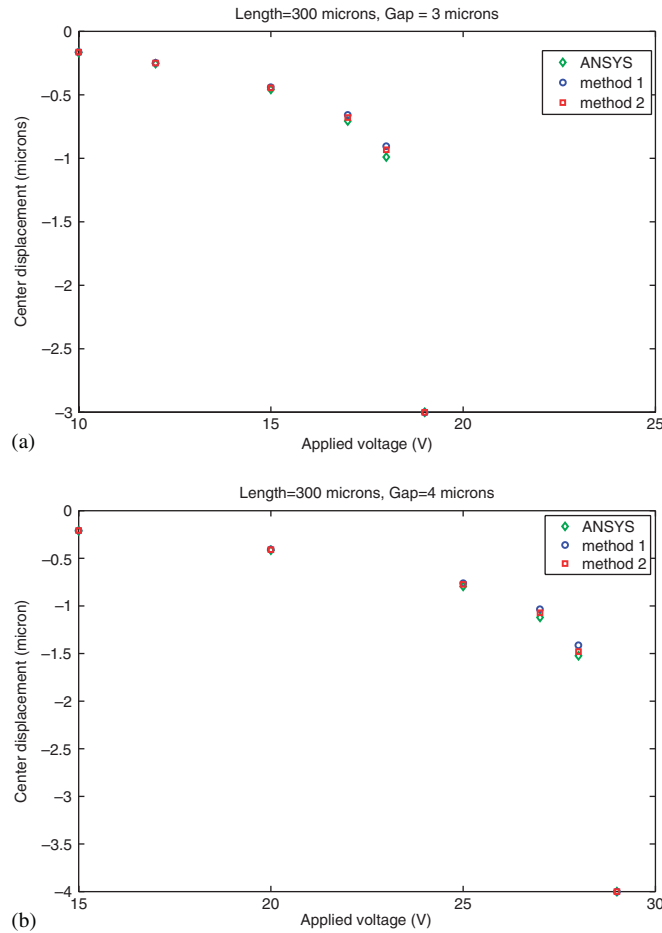


Figure 9. Center deflection of RF MEMS capacitive switch: (a) gap length=3.15  $\mu\text{m}$  and (b) gap length=4.15  $\mu\text{m}$ .

where  $h$  is the thickness of the structure,  $x$  is the transverse displacement of the moving stage and  $V$  is the applied voltage. Plotted in Figure 12 is a comparison between results from the above analytical expressions and those obtained using Method 2. Application of Method 1 for this geometry, while possible, requires the *a priori* identification of the fixed gap lengths for different portions of the moving electrode. In contrast, Method 2 provides an automatic way for their computation. Thus, it is preferable for structures exhibiting substantial geometric complexity, such as in the case of a comb drive.

### 3.4. Torsional micro-mirror

Torsional micro-mirrors have been widely used in applications such as spatial light modulators, optical crossbar switches, adaptive optics and digital projection displays [19,20]. This case study focuses on the application of the proposed method to the electrostatic analysis of

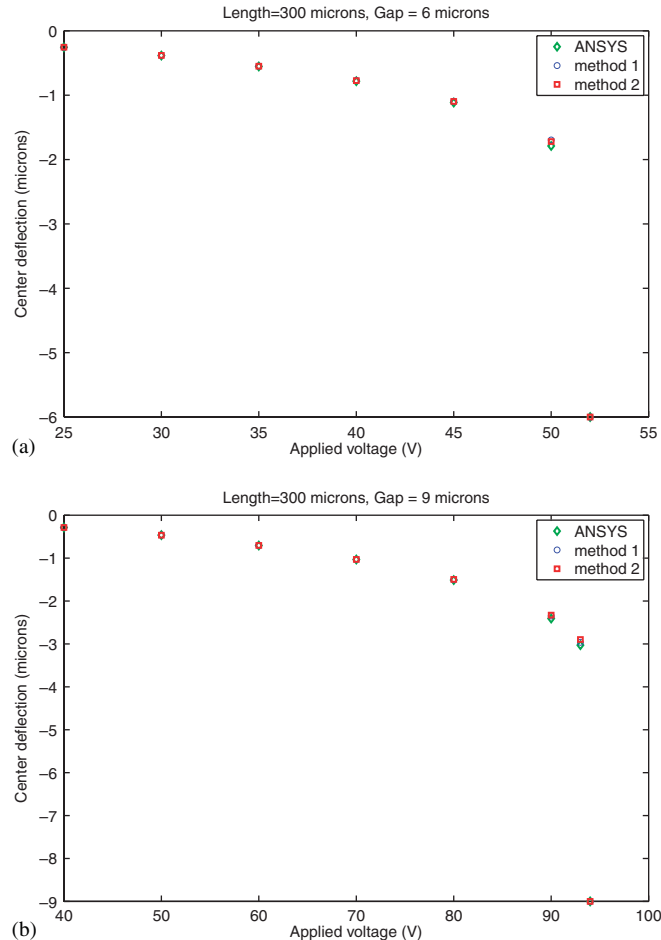


Figure 10. Center deflection of RF MEMS capacitive switch: (a) gap length=6.15  $\mu\text{m}$  and (b) gap length=9.15  $\mu\text{m}$ .

a typical torsion micro-mirror device. Since the device involves rotation of electrodes and thus substantial fringing, it serves as an ideal candidate for assessing the limits of validity of the proposed methodology.

Figure 13(a) depicts a generic version of the most general design of a torsion micro-mirror reported in the literature [19, 21]. It consists of two metal electrodes mounted on a beam that is pivoted at the center. The beam is free to rotate about the pivot. There are two bottom electrodes located at a certain distance below the top electrodes. A voltage applied between two electrodes on one side produces an electrostatic force of attraction between them, which results in a torque on the beam. This torque causes the beam to rotate and rest at an angle to the original position. The most important design parameter of a torsion micro-mirror is the maximum angle of rotation before it snaps and pulls in. This parameter depends on the gap between the top and bottom electrodes and the length of the top beam.

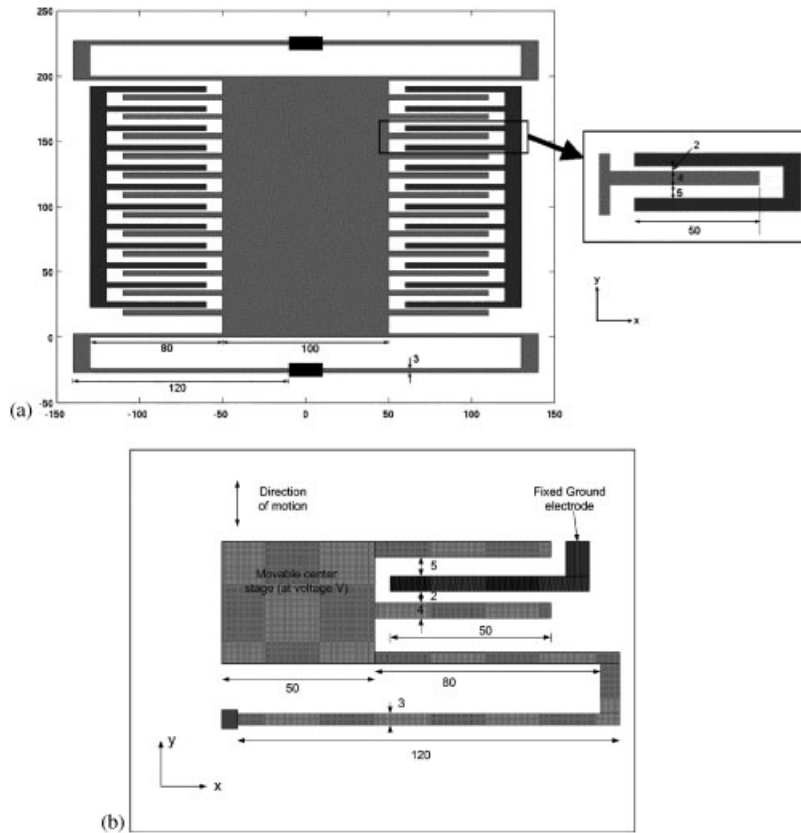


Figure 11. Comb drive: (a) actual design and (b) modeled geometry. All dimensions in microns.

For micro-mirror devices reported in the literature, most length-to-gap ratios are greater than 50:1. However, in order to assess the limits of validity of the proposed method, we consider a design of a micro-mirror with a length-to-gap ratio of 10:1. We consider the state of a torsion mirror just before/at pull-in. In other words, we consider the maximum rotation of the top beam. From [21], the angle  $\alpha$  at which the beam pulls in is given by

$$\alpha = 0.44 \frac{d}{L} \quad (24)$$

where  $d$  is the distance between the top and bottom electrodes and  $L$  is the length of the beam on one side of the pivot.

We apply the proposed method (to the non-deformed configuration Figure 13(a)) to calculate the electric field along the top electrodes and compare the results with those obtained using the conventional FEM analysis for the beam in the deformed configuration (Figure 13(b)). The comparison is shown in Figure 14(a). It is clear that very good agreement is observed. The electric charge density is also computed. The % error in the calculated charge density along the top-left electrode is plotted in Figure 14(b). The maximum error is about 2% and occurs at the extreme left. Along the beam the error is less than 1% demonstrating the accuracy of our proposed method.

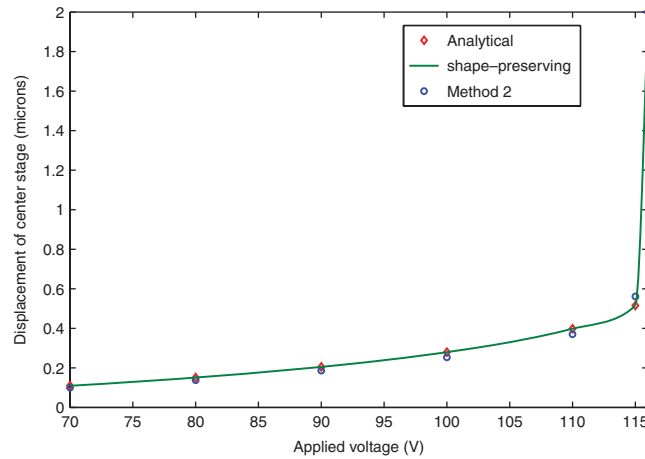


Figure 12. Transverse comb drive: comparison with analytical solution.

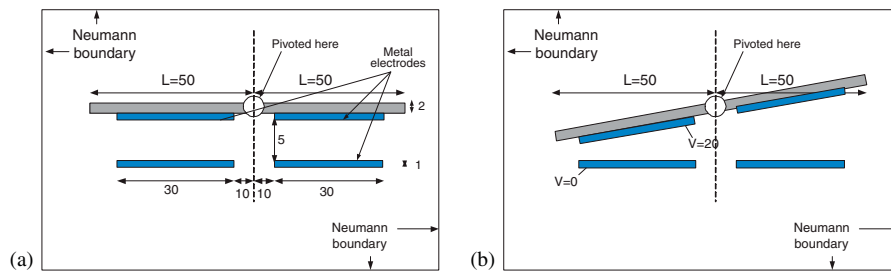


Figure 13. Torsion micro-mirror: (a) undeformed state and (b) deformed state. All dimensions in microns.

#### 4. CONCLUSIONS

In summary, we have proposed a methodology for expediting the coupled electro-mechanical finite element modeling of electrostatically actuated MEMS devices. The enhanced efficiency of the proposed methodology is achieved by eliminating the mesh updating, stiffness matrix calculation, and stiffness matrix factorization, associated with the FEM solution of the electrostatic problem at each step of a relaxation-based algorithm, which is assumed to be used for the electro-mechanical simulation. The way this is accomplished is through the approximate calculation of the charge density on the electrode in the deformed geometry in terms of the charge density on the electrode in the original non-deformed geometry. This definition is based on the ratio of two line integrals along flux lines in the two geometries. The ratio is approximated based on displacements of the movable electrode.

The accuracy of the proposed methodology was examined through its application to the modeling of four classes of MEMS geometries, namely, a cantilever series switch, a simply supported RF MEMS capacitive switch, a transverse comb drive and a torsion micro-mirror. The dimensions and

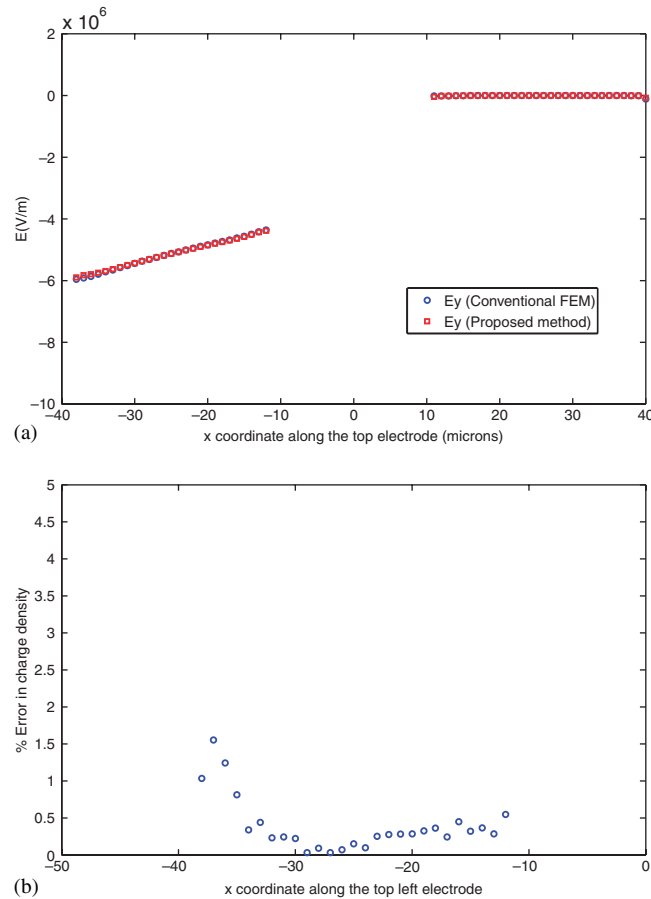


Figure 14. Torsion micro-mirror electrostatic analysis: (a) electric field comparison with conventional FEM and (b) % error in charge density along the top-left electrode.

material properties used for the validation studies were representative of practical MEMS devices. The proposed method is most suitable for such rectilinear geometries. Through comparisons with reference solutions obtained using either FEM electro-mechanical modeling using ANSYS or analytical solutions where appropriate, it was shown that the proposed methodology is accurate for the four classes of the small-displacement, electrostatically actuated MEMS devices considered. This was achieved at an estimated ten-fold reduction in computational cost compared with a standard FEM-based electro-mechanical modeling.

#### ACKNOWLEDGEMENTS

This research was supported in part by the Defense Advanced Research Projects Agency (DARPA), under the N/MEMS Science & Technology Fundamentals Research Program.

## REFERENCES

1. Yao J. RF MEMS from a device perspective. *Journal of Micromechanics and Microengineering* 2000; **10**:9–38.
2. Tillmans H, Raedt W, Beyne E. MEMS for wireless communications: 'from RF-MEMS components to RF-MEMS-SIP'. *Journal of Micromechanics and Microengineering* 2003; **13**:139–163.
3. Goldsmith C, Ehmke J, Malczewski A, Pillans B, Eshelman S, Yao Z, Brank J, Eberly M. Lifetime characterization of capacitive RF MEMS switches. *IEEE MTT-S International Microwave Symposium Digest* 2001; 227–230.
4. Varadan V, Vinoy K, Jose K. *RF MEMS and their Applications*. Wiley: New York, 2003.
5. van Spengen W, Peurs R, Mertens R, Wolf I. A comprehensive model to predict the charging and reliability of capacitive RF MEMS switches. *Journal of Micromechanics and Microengineering* 2004; **14**:514–521.
6. Senturia S, Harris R, Johnson B, Songmin K, Nabors K, Shulman M, White J. A computer-aided design system for microelectromechanical systems (MEMCAD). *Journal of Microelectromechanical Systems* 1992; **1**:3–13.
7. Nabors K, White J. FastCap: a multi-pole accelerated 3-D capacitance extraction program. *IEEE Transactions on Computer-Aided Design* 1991; **10**:1447–1459.
8. Jin J. *The Finite Element Method in Electromagnetics*. Wiley: New York, 2002.
9. Li G, Aluru N. Hybrid techniques for electrostatic analysis of nanoelectromechanical systems. *Journal of Applied Physics* 2004; **96**:2221–2231.
10. De S, Aluru N. Full-Lagrangian schemes for dynamic analysis of electrostatic MEMS. *Journal of Microelectromechanical Systems* 2004; **13**:737–758.
11. Li G, Aluru N. A Lagrangian approach for electrostatic analysis of deformable conductors. *Journal of Microelectromechanical Systems* 2002; **11**:245–254.
12. Soma A, Bona F, Gugliotta A, Mola E. Meshing approach in non-linear FEM analysis of microstructures under electrostatic loads. *Proceedings of SPIE* 2001; **4408**:216–225.
13. Chiandussi G, Bugeđa G, Onate E. A simple method for automatic update of finite element meshes. *Communications in Numerical Methods in Engineering* 2000; **16**:1–19.
14. Zhulin V, Owen S, Ostergaard D. Finite element based electrostatic-structural coupled analysis with automated mesh morphing. *International Conference on Modeling and Simulation of Microsystems* 2000; 501–504.
15. Telukanta S, Mukherjee S. Fully Lagrangian modeling of MEMS with thin plates. *Journal of Microelectromechanical Systems* 2006; **15**(4):795–810.
16. Hamad E, Omar A. An improved two-dimensional coupled electrostatic-mechanical model for RF MEMS switches. *Journal of Micromechanics and Microengineering* 2006; **16**:1424–1429.
17. Imamura T, Katayama M, Ikegawa Y, Ohwe T, Koishi R, Koshikawa T. MEMS-based integrated head/actuator/slider for hard disk drives. *IEEE/ASME Transactions on Mechatronics* 1998; **3**:167–174.
18. Ye W, Mukherjee S. Optimal shape design of three-dimensional MEMS with applications to electrostatic comb drives. *International Journal for Numerical Methods in Engineering* 1999; **45**:175–194.
19. Zhang X, Chau F, Quan C, Lam Y, Liu A. A study of the static characteristics of a torsion micromirror. *Sensors and Actuators A* 2001; **90**:73–81.
20. Buhler J, Funk J, Korvink J, Steiner F, Sarro P, Baltes H. Electrostatic aluminum micromirrors using double-pass metallization. *Journal of Microelectromechanical Systems* 1997; **6**(2):126–135.
21. Degani O, Socher E, Lipson A, Leitner T, Setter D, Kaldor S, Nemirovsky Y. Pull-in study of an electrostatic torsion microactuator. *Journal of Microelectromechanical Systems* 1998; **7**(4):373–379.